The sensitivity of lowermost mantle anisotropy to past mantle convection

James Ward[a,1], Andrew M. Walker[b], Andy Nowacki[a,*], James Panton[c], J. Huw Davies[c]

[a]School of Earth and Environment, University of Leeds, Leeds, LS2 9JT, West Yorkshire, United Kingdom
[b]Department of Earth Sciences, University of Oxford, Oxford, OX1 3AN, Oxfordshire, United Kingdom
[c]School of Earth and Environmental Sciences, Cardiff University, Cardiff, CF10 3AT, Cardiff, United Kingdom

Abstract

It is widely believed that seismic anisotropy in the lowermost mantle is caused by the flow-induced alignment of anisotropic crystals such as post-perovskite. What is unclear, however, is whether the anisotropy observations in the lowermost mantle hold information about past mantle flow, or if they only inform us about the present-day flow field. To investigate this, we compare the general and seismic anisotropy calculated using Earth-like mantle convection models where one has a time-varying flow, and another where the present-day flow is constant throughout time. To do this, we track a post-perovskite polycrystal through the flow fields and calculate texture development using the sampled strain rate and the visco-plastic self-consistent approach. We assume dominant slip on (001) and test the effect of the relative importance of this glide plane over others by using three different plasticity models with different efficiencies at developing texture. We compare the radial anisotropy parameters and the anisotropic components of the elastic tensors produced by the flow field test cases at the same location. We find, under all ease-of-texturing cases, the radial anisotropy is very similar (difference $< 2\%$) in the majority of locations and in some regions, the difference can be very large ($> 10\%$). The same is true when comparing the elastic tensors directly. Varying the ease-of-texture development in the crystal aggregate suggests that easier-to-texture material may hold a stronger signal from past flow than harder-to-texture material. Our results imply that broad-scale observations of seismic anisotropy such as those from seismic tomography, 1-D estimates and normal mode observations, will be mainly sensitive to present-day flow. Shear-wave splitting measurements, however, could hold information about past mantle flow. In general, mantle memory expressed in anisotropy may be dependent on path length in the post-perovskite stability field. Our work implies that, as knowledge of the exact causative mechanism of lowermost mantle anisotropy develops, we may be able to constrain both present-day and past mantle convection.

Keywords: mantle dynamics, seismic anisotropy, post-perovskite

1. Introduction

Mantle convection has played a critical role in shaping the present-day surface environment and its evolution through time. It remains unclear, however, how mantle convection varies spatially and evolves, particularly in the lowermost mantle. Seismic anisotropy offers a unique probe into the convective patterns of the lowermost mantle and has been observed nearly ubiquitously in the enigmatic D″ region (e.g. Wookey et al., 2005; Cottaar and Romanowicz, 2013; Nowacki et al., 2010, 2011; Wolf et al., 2023a). As seismic anisotropy is widely believed to be caused by the gradual alignment of anisotropic crystals during mantle flow (Nowacki and Cottaar, 2021), it may hold information about past and present-day flow.

Several studies have shown the alignment of $MgSiO_3$ post-perovskite (ppv) crystals in D″ from flow-induced strain can cause an Earth-like anisotropy signal (e.g. Wenk et al., 2006; Walker et al., 2011; Wenk et al., 2011; Nowacki et al., 2013; Cottaar et al., 2014; Chandler et al., 2021). These studies calculate their anisotropy from the flow field in approximately the same way. Strain rates experienced along a path through a mantle flow field are measured and used to model texture development in a polycrystal of a particular composition such as $MgSiO_3$ post-perovskite (Hirose et al., 2015) or periclase (Park et al., 2022). This texture is then combined with single-crystal anisotropy elastic tensors to estimate the elastic tensor for the whole polycrystal at the end of the pathline. This modelling approach has been a powerful tool to investigate the cause and controls of anisotropy in the lowermost mantle. Some have used this to study anisotropy in local regions where subducting material is impinging on the core-mantle boundary (Wenk et al., 2011; Cottaar et al., 2014; McNamara et al., 2002, 2003). Others aimed to produce a map of radial seismic anisotropy for comparison with tomographic observations (Walker et al., 2011) and explored the effects of topotaxy (Walker et al., 2018; Chandler et al., 2021). Other studies have predicted the shear-wave splitting (Silver and Chan, 1991) signal from these ppv textures to compare with real observations(Nowacki et al., 2013; Nowacki and Cottaar, 2021). What remains an open question, however, is to what extent seismic anisotropy in the lowermost mantle holds information about past mantle flow, and it is this question we investigate here. In line with the previous studies, we assume lowermost mantle anisotropy is caused by the alignment of ppv crystals but other mechanisms such as

*Corresponding author: a.nowacki@leeds.ac.uk
[1]Now at HM Government Statistical Service

melt inclusions or layering can also cause seismic anisotropy.

Constraining the influence of past flow on present-day anisotropy will allow us to better use anisotropy to constrain the Earth's mantle convection. If anisotropy is mainly impacted by present-day flow, then current flow may one day be inverted from seismic tomography. On the other hand, if anisotropy is sensitive to past flow, then observations of anisotropy may offer unique sensitivity to past mantle convection. To infer the sensitivity of seismic anisotropy to past flow, we compare the anisotropy in D″ calculated with two flow field test cases. In one case, we use the full dynamic flow field history where the flow is allowed to vary with time. In the other case, the present-day flow snapshot is kept constant throughout time. Note both flow fields have the same present-day mantle convection pattern. Previous studies differ in how the texture was generated from the flow fields. Wenk et al. (2011) traced particles to keep track of strain rates experienced along a pathline during forward modelling of the scenario in question such as a subducting slab impinging onto the core-mantle boundary. This approach has the advantage of a higher flow field resolution than a global flow inversion used by other studies (Walker et al., 2011). When tracing particles during forward modelling the final locations of the particles can not be controlled, leaving regions in the model unsampled. In contrast, when tracing the particles backwards in time the final location can be defined, but previously this has required a time-invariant flow field (Walker et al., 2011). In our approach, we get the best of both of these approaches; we use modern mantle convection simulations to create high-resolution global flow fields with Earth-like parameters (Davies et al., 2012a) and have control over where we measure the anisotropy by tracing particles back in time. For this study, a sufficiently Earth-like mantle convection field will have realistic flow velocities, flow velocity gradients and temperatures in the lower mantle. As the model we use has a surface plate motion model, a reasonable viscosity profile and a reasonable core temperature, we argue this model is sufficient for this study.

In line with previous studies (Walker et al., 2011; Nowacki et al., 2010; Walker et al., 2018), we assume anisotropy is created in D″ by the crystallographic alignment of $MgSiO_3$ post-perovskite as several studies have suggested its presence and anisotropic nature (Merkel et al., 2007; Miyagi et al., 2010; Hirose et al., 2015; Kuwayama et al., 2022). As anisotropy is affected by both the strain rates sampled along the particle path and the slip systems of the material being textured, the sensitivity of anisotropy to past flow is also controlled by these mechanisms. Therefore, while our plasticity models always assume deformation is dominantly accommodated along (001), we construct three different sets of slip system activities which cause texture to develop with different efficiencies to test this effect.

Our results provide a conservative estimate of the extent to which past flow is observable in seismic anisotropy. We find that global, present-day mantle convection dominates anisotropic signal in D″, but in many regions past mantle flow is recorded. Therefore, localised observations such as shear-wave splitting (Silver and Chan, 1991) and body wave waveform studies may be able to discriminate between models of mantle convection history. Broader scale observations such as from seismic tomography will mostly be sensitive to present-day flow and could be used to invert for mantle flow.

2. Methods

This study aims to test the sensitivity of present-day anisotropy (the full elastic tensor) to past mantle flow in D″ assuming it is caused by texturing of post-perovskite-rich material. To test the memory of seismic anisotropy, we use a fully-dynamic model of mantle convection and create an Earth-like mantle flow field history (Section 2.1). From this, we create two flow field cases: one where mantle flow changes with time, and the other where the flow at the present day is kept constant through time. Note the flowfield we use as the 'present-day' flowfield is that at the end of the mantle convection simulation. As anisotropy is also sensitive to the slip systems of the material being textured, the impact of past flow on present-day anisotropy may also be affected by these slip systems. Therefore, we also vary the slip systems of post-perovskite and create three ease-of-texturing test cases, all with dominant slip on (001). The resulting anisotropy is analysed to determine the effect of past flow on present-day anisotropy and whether an easily textured material dampens or enhances this effect.

2.1. Mantle convection model

We use TERRA (Baumgardner, 1985; Bunge et al., 1997; Davies et al., 2012b; Panton et al., 2023), a three-dimensional mantle convection code, to solve the governing equations with the Boussinesq approximation and assume an incompressible mantle (McKenzie et al., 1974). Driving parameters for the simulation are listed in Table 1. The model domain is discretised into 129 radial layers with an average radial spacing of ∼22.5 km. In each of these layers, we form a grid by projecting a regular icosahedron projected onto a sphere. The grid is equally discretised at each layer resulting in an average lateral grid spacing of ∼16 km at the core-mantle-boundary (CMB) and ∼30 km at the surface. The surface boundary is isothermal (300 K) and has lateral velocities applied from plate motion reconstructions since the beginning of the Neoproterozoic (Merdith et al., 2020). As such, the model features hot ridges, plumes and cool subduction zones where surface material is recycled into the mantle. The CMB boundary is also isothermal (3000 K) and is free-slip. The CMB boundary temperature is lower than current seismological and mineral physics estimates for CMB temperature (Kim et al., 2020; Lobanov et al., 2021; Deschamps and Cobden, 2022) due to the incompressible equation of state that we use. A theoretical adiabat is added to account for compressibility when using the temperature field to calculate post-perovskite stability. The adiabat is calculated using a linear increase in temperature in the upper mantle (until 660 km depth) and then fit to a quadratic increase in the lower mantle.

As well as heating from the bottom boundary, the model is internally heated via the decay of radioactive isotopes, concentrations of which are tracked using tracer particles. A depth and composition-dependent solidus controls melting (van Heck

Table 1: Driving parameters for the simulation. Reference viscosity is equal to the viscosity of the upper mantle.

Symbol	Parameter	Value	Unit
T_S	Surface temperature	300	K
T_{CMB}	CMB temperature	3000	K
η_0	Reference Viscosity	3×10^{21}	Pa s
ρ_0	Reference Density	4500	kg m^{-3}
k	Thermal conductivity	4	W m^{-1} K^{-1}
α	Thermal expansivity	2.5×10^{-5}	K^{-1}
C_p	Specific heat capacity	1100	J kg^{-1} K^{-1}

et al., 2016), which occurs at ridges and plume heads, causing heat-producing elements to be fractionated. We employ a depth-dependent viscosity with a ~100 km thick lithosphere which is 100 times more viscous than the reference. Note that there is no temperature dependence in the viscosity. Upper mantle viscosity is equal to the reference and a 30-fold jump in viscosity occurs across the bottom of the mantle transition zone at 660 km depth (van Keken and Ballentine, 1998). Viscosity drops off in the bottom 150 km of the mantle to simulate the drop in viscosity across the post-perovskite transitions which occur there (Li et al., 2014).

For the purposes of our study, it is important that we have features in our simulated mantle which are of a similar scale to those found in Earth. The mixed heating Rayleigh number for the simulation is 8.8×10^8, which is in line with estimates for Earth's mantle (Bunge et al., 1997). In our simulation, the mantle cools at a rate of 70 K Gyr^{-1} which is in good agreement with estimates of Earth's mantle cooling rate (Labrosse and Jaupart, 2007). At the present day, the surface heat flux in the model is 40.5 TW, only slightly higher than current estimates for Earth's mantle heat flux (Davies and Davies, 2010). All of this gives us confidence that our simulation is thermally behaving in a similar way to the Earth and so should produce thermal features which are recognisably Earth-like. Fig. 1 shows the temperature and radial flow fields in the lower mantle as well as the predicted post-perovskite thickness. Although Earth-like, it is unlikely that this model will perfectly capture the finest properties of mantle convection. As we are comparing the flow field models to each other, a mantle convection model with the properties described above is suitable for our purposes.

2.2. *Predicting anisotropy from flow fields*

We calculate anisotropy in the lowermost mantle from the flow fields in a similar way to Walker et al. (2011) with the addition of allowing for a time-varying flow field. We give a brief summary of the methodology and explain the addition of a time-varying flow field.

The flow field is taken from the mantle convection model outlined in Section 2.1. For each point of interest, we trace a particle backwards through time in the flow field using 4th-order Runge-Kutta integration with a constant time step of 25,000 years. This timestep gives very similar results to that of a time step of 5000 years. For computational efficiency, the flow velocities and time step can be scaled by a further constant factor, meaning fewer individual steps are needed; here we use a factor of 10 which on average gives the same elasticity as using a factor of 1 (no scaling). Note that for a time-constant flow field, we will be tracing streamlines through the final flow field snapshot whereas in the time-varying case, we will be tracing path lines using multiple flow field time snapshots. The particle continues to be traced back through time until it reaches the phase transition between post-perovskite and bridgmanite. Whether there is a phase transition at that location is determined using the pressure and temperature at the location and a Clapeyron slope of 7.0×10^{-3} MPa K^{-1} and pressure intercept of 105.7 GPa. The predicted post-perovskite thickness in the model is shown in Fig. 1c. The pressure is calculated using the density from 1-D Earth model ak135 (Kennett et al., 1995) and temperature from the model's temperature field.

At each step along the path, we extract the velocity gradient tensor and use this to calculate the textural evolution of a post-perovskite polycrystal. The evolution of the polycrystal needs to model the rotation and alignment of all the crystals in the aggregate. Rather than describing all interaction between adjacent crystals, we use the visco-plastic self-consistent (VPSC) approach (Lebensohn and Tomé, 1993). VPSC represents adjacent grain interactions by embedding each grain in a homogeneous medium which represents the other grains in the polycrystal. For the velocity gradients to be translated to the rotation and deformation of the polycrystal, we assume material properties of post-perovskite in the form of slip system activities. The slip systems impact the texture development along the path and also the final anisotropy. Therefore, to investigate the influence of past flow on anisotropy, we need to investigate the effect of different slip systems. This is done by varying the slip system activities such that the ease of texture development is varied.

To calculate the texture, we use 500 post-perovskite crystals which are randomly oriented at the beginning of each path. This reflects that in this study we assume no texture is inherited in post-perovskite when it transforms from bridgmanite, or that bridgmanite does not form a texture. At the end of the pathline, the crystals have been rotated. From these orientations, we calculate the elastic tensor of the polycrystal by computing the Voigt–Reuss–Hill average over all crystal orientations and the single-crystal elastic tensor. Here, we use single-crystal properties found by Stackhouse et al. (2005) and Stackhouse and Brodholt (2007) interpolated in pressure-temperature space with the approach described by Ammann et al. (2010) using pressure derivatives from Wentzcovitch et al. (2006). We assume the effect of different pressure and temperature on the single-crystal anisotropy is small relative to other actors in the model affecting the anisotropy such as the flowfield or slip system activities, in line with previous studies (Walker et al., 2011). From this elastic tensor, the radial anisotropy parameters $\xi = V_{SH}^2/V_{SV}^2$ and $\phi = V_{PV}^2/V_{PH}^2$ can be calculated and compared. Alternatively, the elastic tensors between the time-constant and time-varying cases can be compared directly. This approach means the final anisotropy is an accumulation of texturing along the whole path but, crucially, the importance of past texturing is uncertain.

To allow the flow field to vary with time, we take flow field

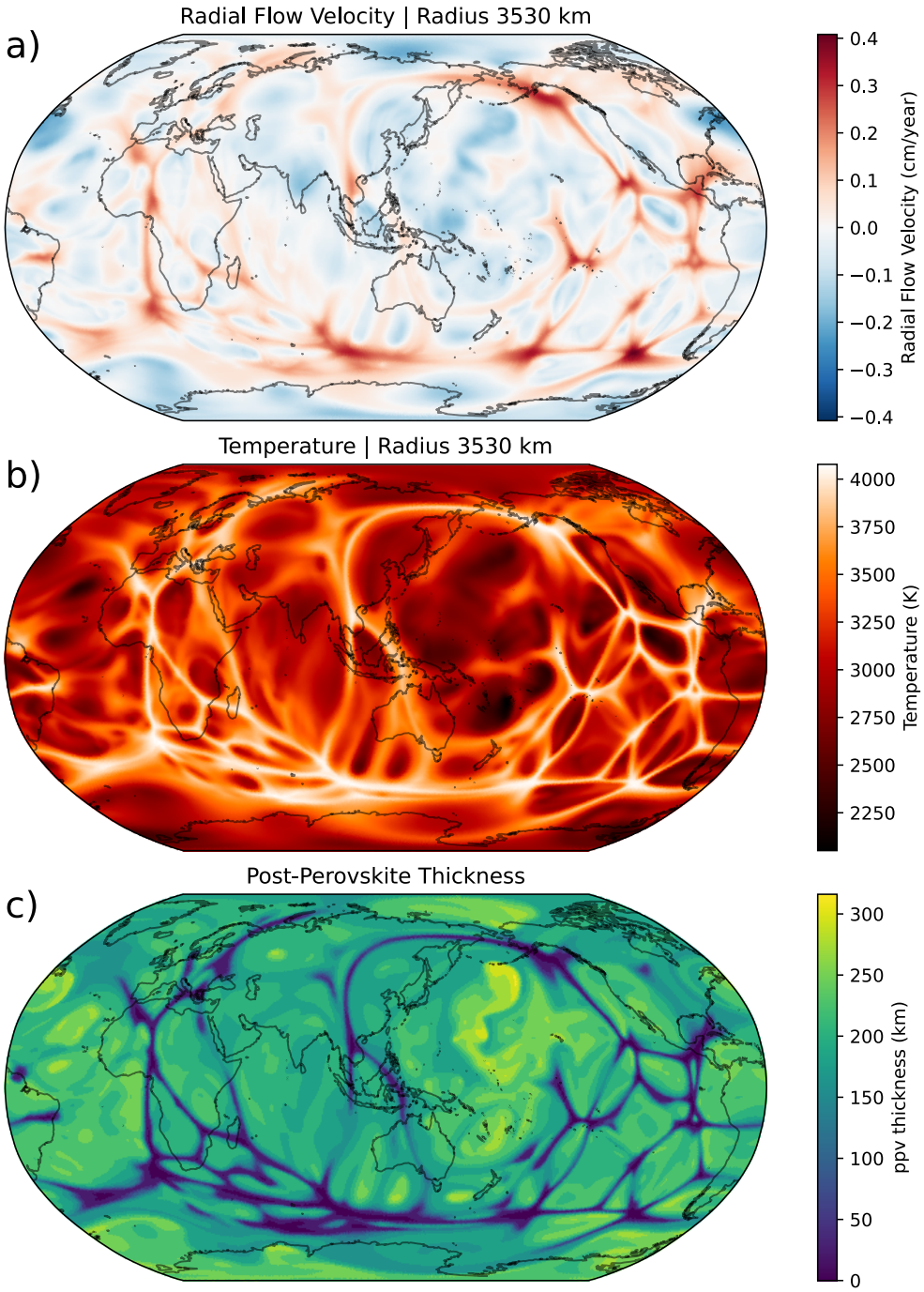

Fig. 1: Present-day (end of mantle convection simulation, 0 Ma) summary snapshot of the mantle convection model used in this study showing (a) radial flow velocity, (b) temperature (with adiabat added), and (c) post-perovskite thickness. Notice that upwelling, high-temperature regions also have very thin or no post-perovskite and mark areas of convergent flow.

Table 2: Table showing the relative critical resolved shear stress (CRSS) coefficients used in VPSC for the different ease-of-texture cases. Each of these accommodates strain along the 001 plane as observed by Miyagi et al. (2010). The different models represent different scenarios for how easily texture develops in the post-perovskite polycrystal. Slip systems not listed do not accommodate any strain.

	Ease of texture development		
Slip System	Hard	Medium	Easy
[100](001)	1	1	1
[010](001)	1	1	1
[001](100)	3	5	10
[010](100)	3	5	10
[001]{110}	3	5	10
⟨110⟩(001)	2	2	2
⟨110⟩{110}	3	5	10

snapshots at 10 Ma intervals and linearly interpolate between them for intervening times. We use 4th-order Runge-Kutta integration to find the new location of the particle based on the flow velocities at its current location and time. The spatial gradient of the flow field is calculated and a new particle location is found using the time-interpolated flow field. This process is repeated until the particle reaches the phase transition from post-perovskite to bridgmanite. Note that because the particles are traced until they hit the phase transition, each particle accrues texture in D″ over a different distance (between 0 km and 8000 km; Fig. 3) and length of time (between 0 Ma and 120 Ma). If the final location of the particle is not in the post-perovskite stability field, no anisotropy is calculated and plotted in grey later in Section 3.

2.3. Test setup

To explore the dependence of present-day anisotropy on past mantle flow, we perform the texture development calculation described above on an equal-area grid approximately 50 km above the core-mantle boundary. The grid was created using the healpix algorithm (Gorski et al., 2005). The resulting anisotropy, and therefore its sensitivity to past flow, is controlled both by the strain rates sampled along the path and the slip system activities of the material being textured.

We use the flow field from the model described in Section 2.1 and perform the analysis in two cases. In the first case, the flow field is time-constant and we trace particles as streamlines through the present-day flow field. In the other case, the flow field is time-varying and we trace the particles as path lines through the whole dynamic history. We use the present-day flow as the constant-through-time case because it is common for seismic anisotropy observations to be interpreted in the context of present-day flow only. To predict elastic anisotropy, we need to assume the ppv slip system activities which can impact the final anisotropy and therefore the impact of past flow on such anisotropy. We use three slip system cases where we vary how easily the ppv aggregate develops texture and allow the texture to develop on the 001 plane. The slip systems activities are listed in Table 2.

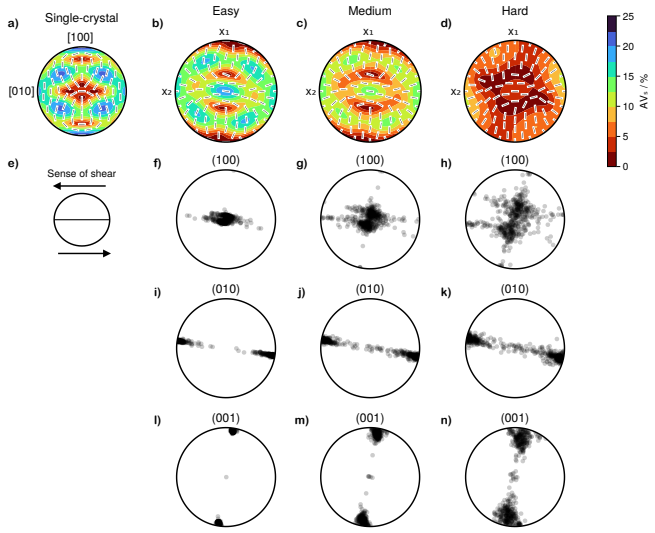

Fig. 2: Texture development in the three plasticity models used in this study for simple shear (top to the left) up to a shear strain $\gamma = 2$. (a) Shear-wave anisotropy of single-crystal $MgSiO_3$ post-perovskite (ppv) at 125 GPa and 2500 K (Stackhouse et al., 2005; Stackhouse and Brodholt, 2007). (b–d) Shear wave anisotropy for the deformed ppv aggregates for the easy (b), medium (c) and hard (d) plasticity cases. Orientation of the fast shear wave are shown as black ticks, while $AV_S = 200(V_{S1} - V_{S2})/(V_{S1} + V_{S2})\,\%$, and S1 and S2 are the fast and slow shear waves, respectively. (e) Diagram showing the sense of shear for this example. (f–n) Directions of poles to planes (f–h) (100), (i–k) (010) and (l–n) (001) for the easy (f, i, l), medium (g, j, m) and hard (h, k, n) models. All figures are upper hemisphere Lambert equal-area diagrams.

To illustrate the different rates at which the three ease-of-texturing plasticity models in Table 2 develop texture, we show the results of VPSC simulations which deform ppv aggregates of 500 grains in simple shear up to a shear strain of 2 in Fig. 2. It is clear that while all three aggregates develop texture in a similar pattern, the strength of texture is different as expected from the plasticity models, and leads to stronger shear wave anisotropy along any given direction for the 'easy' model for the same strain.

We first analyse differences between the flow fields using summary statistics of the paths such as path length and path tortuosity. This shows the difference a time-varying flow field can have on the paths and the sampled strain rates. Then, we compare the anisotropy outputs between the flow fields for each of the ease-of-texturing scenarios. We do this both in terms of radial anisotropy parameters ξ and ϕ and the anisotropic components of the elastic tensor to infer the relative impacts on different observations. At present, lower mantle radial anisotropy is still challenging to constrain accurately with seismic tomography (Chang et al., 2014). Future tomography models may provide useful broad-scale observations of lowermost mantle anisotropy, therefore it is important to know if these observations are impacted by past mantle flow. Before calculating the misfit between elastic tensors C_{ij}, we remove the isotropic component (C^{iso}; Browaeys and Chevrot, 2004) as we only want to compare the difference in anisotropy, leaving the tensor without isotropic part $\hat{C}_{ij} = C_{ij} - C^{\mathrm{iso}}_{ij}$. In a similar way to that done

by Magali et al. (2021) in comparing elastic tensors to compute a loss function, we calculate the misfit as an L_2 norm of the component-wise difference with

$$\text{misfit} = \sqrt{\sum_{ij} (\hat{C}_{ij}^{TV} - \hat{C}_{ij}^{TC})^2}, \quad (1)$$

where $\hat{C}_{ij}^{TV}$ is the elastic tensor produced by the time-varying flow field with the isotropic part removed, and $\hat{C}_{ij}^{TC}$ is the tensor (also with isotropic component removed) for the time-constant flow field. We use Voigt matrix representations of the elastic tensors (a 6×6 matrix) where ij are the indices of the matrix notation we use. Such a misfit is an attempt to capture the size of variation in elasticity between tensors without having to fully reproduce large volumes of seismic data synthetically in these models, which Nowacki and Wookey (2016) showed requires expensive finite-frequency calculations.

From the misfits for each texturing scenario, we can infer the influence of past flow on present-day anisotropy, the impact of ease-of-texturing, and what controls the size of the misfit.

3. Results and interpretation

In this section, we first compare the path length and path tortuosity to analyse the effect a time-varying flow field can have on particle paths. Then, for each of the ease-of-texturing scenarios, we compare the anisotropy between the flow field scenarios. To compare the anisotropy, we analyse the difference between the anisotropic components of the elastic tensors to infer the impact of past flow on measurements that are sensitive to different parts of the elastic tensor such as shear-wave splitting. Then, we use the radial seismic anisotropy values to infer the sensitivity of seismic tomography observations to past mantle flow.

3.1. Path differences

The paths taken by particles through a flow field have a direct impact on the anisotropy at the end of the path. If the path line through a time-varying flow field is different to a streamline through the present-day flowfield, it motivates exploring whether the anisotropy is also different. Here, we explore how different, if at all, the path properties are between the different flow field cases. The properties we compare are the total path length and the tortuosity. Tortuosity is defined as a ratio between the path length and the linear distance between the start and end points of the path. Essentially it is a measure of how non-linear the path is. Fig. 3 shows the length of the paths in the post-perovskite stability field in the time-constant and time-varying cases, as well as the difference between them. It shows, for the majority of locations, the path lengths are very similar (<500 km). In some regions, a time-varying flow field can lead to significantly longer or shorter paths with some differences going up to 6000 km. Analysing the tortuosity tells a similar story (Fig. 4) with the majority of locations showing negligible differences and some locations having very large differences. The difference in tortuosity shows that not only are the paths

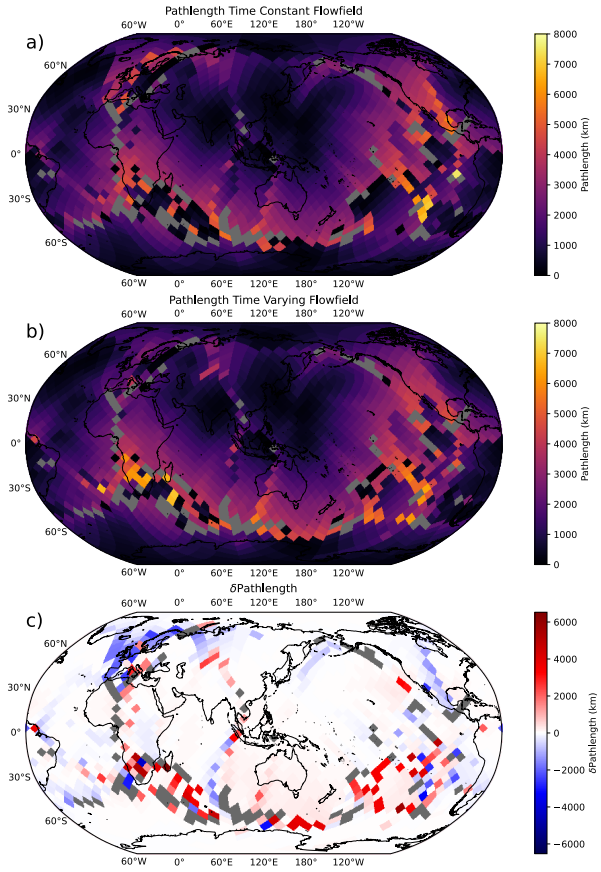

Fig. 3: Maps comparing the path lengths in the ppv stability field ending at each location at 3530 km radius for (a) the time-constant flow field, (b) time-varying flow field and (c) the difference in the length of paths.

longer or shorter but also that the linearity of the paths changes. This comparison shows that a time-varying flow field can significantly affect the paths taken by particles. In the next section, we present the differences in general and seismic anisotropy for the different flow fields.

3.2. Anisotropy comparison

As shown, a time-varying flow field can significantly alter the paths of particles. To predict the anisotropy from these paths, we need to assume the slip system activities of ppv which may also impact the sensitivity of such anisotropy to past flow. In this section, we investigate the spatial distribution of the differences in general and radial anisotropy of the flow fields for each of the ease-of-texturing models.

3.2.1. General anisotropy

As described in Section 2.3, we compare the general anisotropy between the flow field test cases by taking the misfit between the elastic tensors at the same locations. Fig. 5 shows a map of the misfits for the three ease-of-texturing cases. In the majority of locations, for all ease-of-texturing cases, the difference is small (< 50 GPa), however, in some local regions, there are very large differences (> 300 GPa). For context, a 50 GPa difference is equivalent to the misfit between two ppv crystals

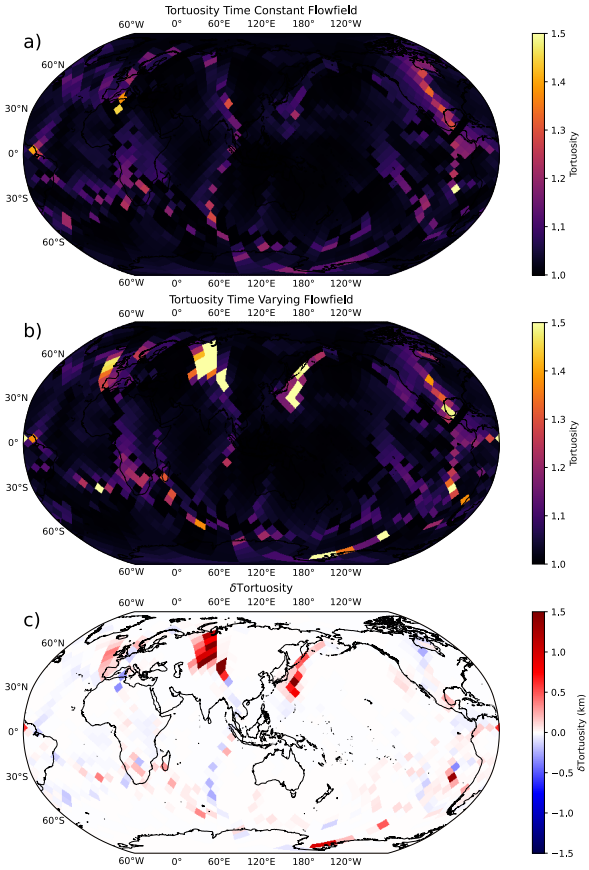

Fig. 4: Maps comparing the tortuosity in the ppv stability field ending at each location at 3530 km radius for (a) the time-constant flow field, (b) time-varying flow field and (c) the difference in the length of paths.

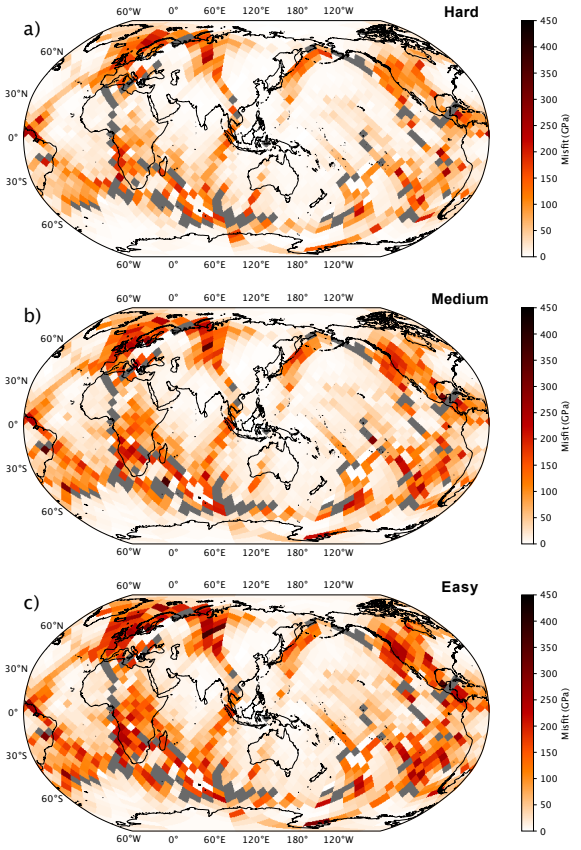

Fig. 5: Maps showing the distribution of misfit values between the elastic tensors calculated with a time-constant and with a time-varying flow field for the three ease-of-texturing scenarios at 3530 km radius, (a) the 'hard' case, (b) 'medium' and (c) 'easy'. The regions in grey show where post-perovskite is not stable. Notice the easier-to-texture case has more locations with a very high misfit (>350 GPa).

with properties from Stackhouse et al. (2005) where one is rotated by less than 15 ° around the b axis. A 300 GPa difference is equivalent to comparing the two ppv crystals where one is rotated by approximately 45 °.

Visual inspection of Figs. 3, 4, and 5 suggests a relationship between the differential path measures earlier (path length and tortuosity) and general anisotropy misfit. We quantitatively investigate this possible relation by plotting the misfit and the path parameters and calculating the Spearman correlation coefficient (Fig. 6). We also investigate the possible contribution of temperature at the end of the path and the influence of past flow.

We find a positive correlation between the difference in path length and the misfit values (0.54). The same is true for the difference in tortuosity (0.55). This reinforces our suggestion that the differences in the paths contribute to the differences in anisotropy between the flow fields. There is also a weak but positive correlation between the misfits and temperature (0.27) suggesting some relationship between hotter regions and the impact of past flow exists, but it is not as important as differences in path properties. We also test how predictable the differential anisotropy between time-varying and time-constant flow fields is using only the path length (Fig. 6d). We find a

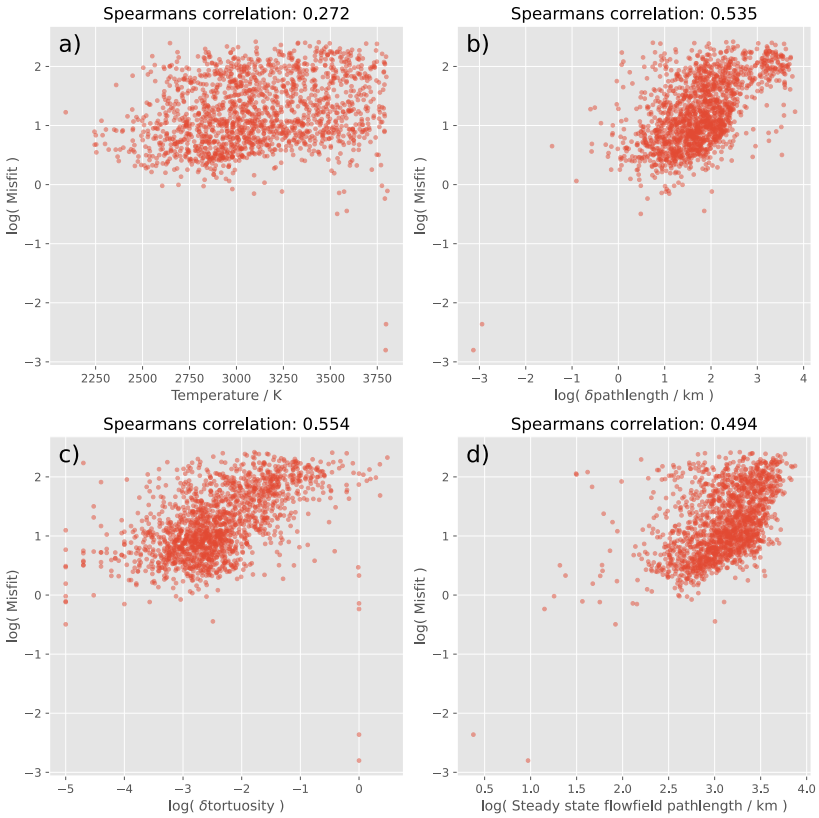

Fig. 6: Scatter plots of the misfit between elastic tensors and parameters which may impact how much past flow affects the anisotropy at a location, for the hard-to-texture case. Panel (a) compares misfit with the temperature, (b) with the difference in path length, (c) with the difference in tortuosity, and (d) with the path length in the time-constant model. In panels (b), (c), and (d) we take the logarithm of the model parameters. The Spearman correlation value is shown in the title.

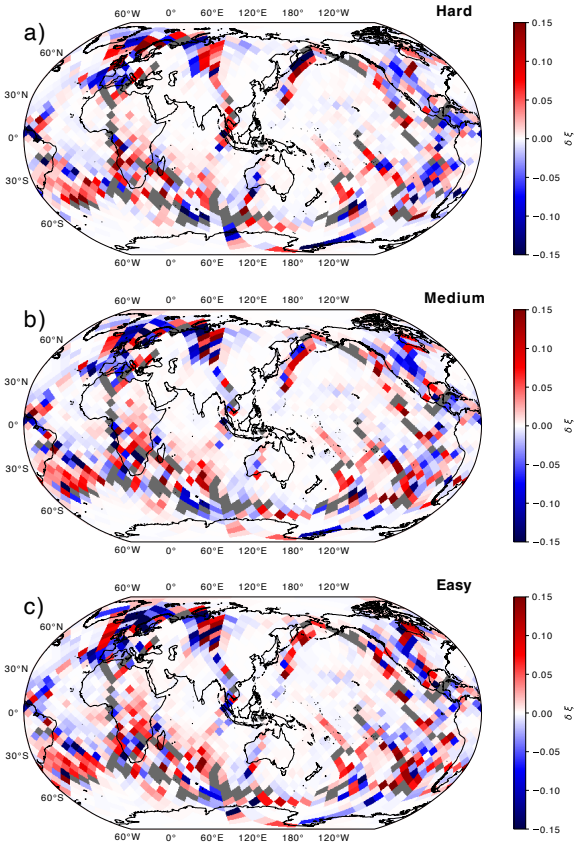

Fig. 7: Maps showing the difference between shear-wave radial anisotropy at 3530 km radius (50 km above the core–mantle boundary) for the different flow fields with the different ease-of-texturing cases, (a) the 'hard' case, (b) 'medium' and (c) 'easy'. The regions in grey show where post-perovskite is not predicted to be stable at this depth.

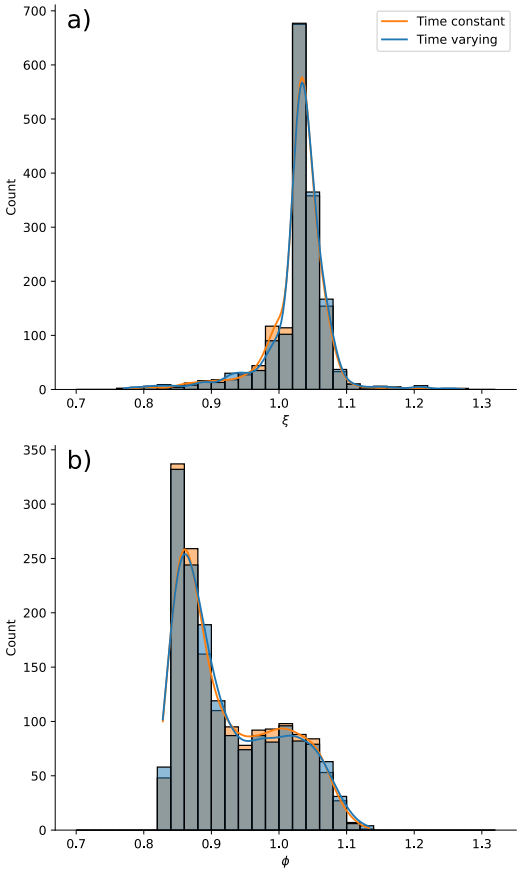

Fig. 8: Histograms of S-wave (a, ξ parameter) and P-wave (b, ϕ parameter) radial anisotropy coloured by whether the flow field was time-dependent or time-constant. The orange and blue lines are the kernel-density estimates for the two cases. Here we can see very little difference between the two for either P- or S-wave radial anisotropy. The lines show the kernel density estimates for the distribution of radial anisotropy for the time-varying and time-constant cases. Note this is for the hard-to-texture case and other texturing cases show equally similar distributions between time-varying and time-constant flow fields.

positive correlation (0.49) between path length and misfit suggesting the longer paths tend to also be more sensitive to past flow.

3.2.2. Radial anisotropy

In addition to comparing the elastic tensors directly, we compare the radial seismic anisotropy predicted by the flow fields for the different ease-of-texturing cases. We do this to test whether observations of radial anisotropy such as those derived from seismic tomography hold information about past flow. A map of the difference in radial anisotropy parameter ξ between the flow models is shown in Fig. 7 for each of the texturing cases. The predicted S and P wave radial anisotropy for the flow field cases and their differences for each ease-of-texturing case are shown in Supplementary Figs. S2 to S7. As with the general anisotropy, the majority of locations have small differences ($< 1\%$), however, in some local regions, there are very large differences ($> 10\%$). We define the percentage anisotropy as $100(\xi - 1)\,\%$. As with our interpretation of the general anisotropy, we hypothesise the large differences are caused by differences in the particle paths (Fig. 3). The distribution of the difference in ϕ tells a similar story (see Supplementary Fig. S1).

The distributions of radial anisotropy for the flow fields are very similar (Fig. 8). Furthermore, the mean values are very similar where ξ has a difference of 0.14 % and ϕ a difference of 0.03 % for the hard-to-texture case (Table 2). The distributions for the other ease of texturing cases show the same pattern. Both the mean ξ ($\sim$ 2.8 %) and ϕ ($\sim$ −7.3 %) indicate horizontally polarised P and S waves travel faster in D″ in our models. Because of the free slip boundary condition, we expect flow near the core-mantle-boundary to be near horizontal. This then causes 001 planes in the post-perovskite aggregate to be broadly horizontal for the 001 slip system and therefore, on average, to cause horizontally polarised waves to travel faster.

The similar mean radial anisotropy in the models, in the context of the spatial similarity also, suggests that in most of the lowermost mantle, radial seismic anisotropy measurements are sensitive to present-day flow only.

3.3. The effect of ease-of-texturing on past flow influence

In addition to exploring the effects of particle path differences, we explore how the ease of texturing of the crystal aggregate affects the impact of past flow on present-day anisotropy.

We do this by comparing the distributions of the elastic tensor misfit (Section 3.2.1) between the ease-of-texturing cases.

In Fig. 9a, we show the distribution of all the misfit values for each of the three texturing cases. We observe the easy-to-texture case having larger misfits than the hard-to-texture case suggesting sensitivity to time variations in flow is affected by the material being textured. Specifically, an easy-to-texture crystal aggregate will hold more texturing from past flow than a hard-to-texture crystal aggregate. This is supported by Fig. 9(b) where there are significantly more misfits in the <10 GPa bin in the hard-to-texture case. Analysing the radial anisotropy (see Supplementary Figs. S8 and S9), shows the same pattern and therefore has the same implications for interpreting observations such as seismic tomography.

We suggest easier-to-texture polycrystals hold more texturing from past flow in our setup because of the difficulty to re-texture a heavily shear-strained polycrystal. If the polycrystal experiences high strain rates early in its path, an easy-to-texture material will be heavily textured and geometric hardening, where the material hardness increases with plastic deformation (Hansen et al., 2012; Mameri et al., 2019), will make new texturing more difficult.

4. Discussion

As the previous sections show, for most locations in the lower mantle of an Earth-like mantle convection model, seismic anisotropy is mostly sensitive to the present-day flow field. In this section, we discuss the implications of these results both for those making observations and also for those investigating the material properties of post-perovskite. Then, we highlight limitations in our modelling approach.

4.1. Implications for seismic anisotropy studies

We have shown in the majority of locations in the lower mantle, seismic anisotropy is sensitive primarily to the present-day flow field, but in small regions, the past flow has a strong influence. Therefore, the implications our findings will have depend on the resolution and location of the seismic anisotropy. Global-scale observations such as 1-D seismic anisotropy observations (De Wit and Trampert, 2015), current body-wave seismic tomography (e.g. Simmons et al., 2021; Auer et al., 2014) or normal-mode observations (Restelli et al., 2023) should be sensitive mainly to present-day flow only in the lower mantle. Note that in the case of seismic tomography improvements in resolution may lead to sensitivity to past flow. Regional-scale observations from shear-wave splitting (e.g. Nowacki et al., 2010; Asplet et al., 2020; Wolf et al., 2023a; Wookey et al., 2005) may be sensitive to present-day flow but potentially could have information about past mantle flow. To investigate whether shear-wave splitting observations have information about past flow, future studies using them to infer flow can compare the observations to those made from flowfield test cases with time-varying and time-constant flowfields. This could potentially constrain what historic flow was like. Future studies could also take existing databases of splitting observations in D″ (e.g. Wolf et al., 2023b) and compare

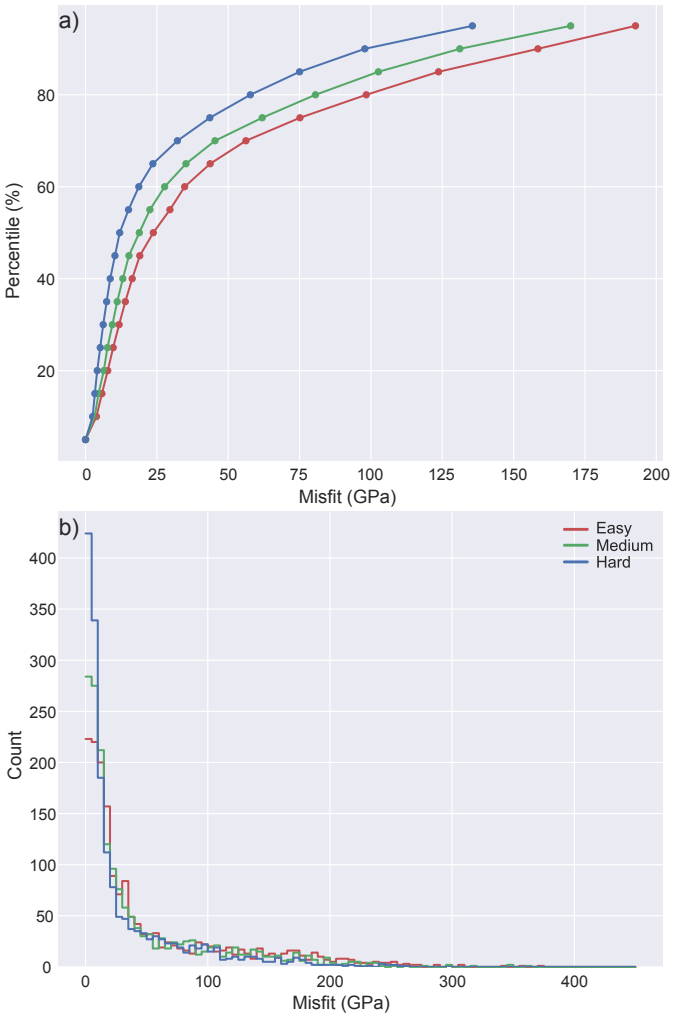

Fig. 9: The effect of slip system activities on sensitivity to past flow. (a) Cumulative histogram of misfit values coloured by the slip system label from Table 2. (b) Simple histograms for misfit data, also coloured by the slip system activities.

them to predictions of different global flowfields to constrain what past flow fields may have been like in the lower mantle.

We found a positive but weak correlation between temperature and elastic tensor misfit (Fig. 6), suggesting seismic anisotropy measurements in hot regions may hold more information about past flow. We believe this weak correlation is caused by differences in path lengths (Fig. 3). The hot regions have different path lengths because of the thin post-perovskite present. Therefore, some paths may be very short and paths between the time-varying and time-constant flowfields could be significantly different and have different texturing history. Stronger correlations with other metrics such as path length show multiple factors contribute to the sensitivity to past flow.

The longer paths in the time-constant flow field tend to also be more affected by a time-varying flow field than the shorter paths (Fig. 6). This may be because there is more opportunity for the particle paths in the different flow fields to deviate, and thus the histories of strain rates likewise tend to diverge. When interpreting regional observations such as those using shear-wave splitting, it is most likely that a time-varying flow field must be considered, with particular caution being taken with longer paths.

We have shown that to be able to interpret lower mantle seismic anisotropy observations in terms of a time-varying flow field, it is vital to know how easily lowermost mantle minerals are textured. We found that harder-to-texture crystal aggregates hold less information about past mantle flow than easier-to-texture crystal aggregates.

4.2. Modelling assumptions

Our results suggest broad-scale observations of seismic anisotropy in the lower mantle such as those from current seismic tomography or 1-D estimates should be sensitive to present-day flow only. On the other hand, higher resolution observations such as shear-wave splitting may hold information about past flow depending on the region sampled. Our model setup is built upon several assumptions and limitations which we discuss here.

A significant assumption we make is assuming deformation in D$''$ is accommodated solely by dislocation creep everywhere. In lowermost mantle conditions, it is likely that other deformation mechanisms are taking place which may or may not result in the texturing of a crystal aggregate. It is unclear what deformation mechanisms are present in the lower mantle, what effect they have on texturing and where they occur. It is commonly believed diffusion creep is present in hot regions, but whether this leads to texture loss (McNamara et al., 2001, 2002), texture preservation (Wheeler, 2009) or continued texture development (Dobson et al., 2019) is debated. Other mechanisms such as pure dislocation climb creep (Boioli et al., 2017; Reali et al., 2019) may be present and result in no texture development, but again, where this happens in the lower mantle and what proportion of deformation is accommodated by this remains uncertain. These will certainly affect the sensitivity of seismic anisotropy to time-varying flow. Our approach means we have essentially maximised the sensitivity of texturing to flow and therefore also maximised the influence of past flow. In light of this, our setup maximises how much past flow influences present-day anisotropy observations. The likely effect of considering other deformation mechanisms is a reduction in the time-sensitivity of seismic anisotropy. To properly account for other deformation mechanisms, more information about the conditions where they dominate and the effect they have on texturing is needed.

Another limitation is there is no cap on texture strength such as that expected to occur from dynamic recrystallisation as dislocation density increases. Not limiting texture strength in our model may lead to geometric hardening where high CPO intensity becomes harder to texture further as has been previously shown in olivine (Hansen et al., 2012; Mameri et al., 2019), which could limit the formation of future texture. Capping texture strength with some form of dynamic recrystallisation or in an ad-hoc way by reducing the velocity gradient magnitude at each step along the path (e.g. Wenk et al., 2011; Cottaar and Romanowicz, 2013) most likely will reduce the sensitivity to past flow and reduce the number of locations where there are large differences between a time-constant and time-varying flow field. As we observe differences between the flow field of up to 15 % radial anisotropy we do not expect reducing the strain rates in an ad-hoc way will greatly change our conclusions.

In our setup, we assume deformation occurs in pure post-perovskite and there is no texture inheritance from deformation outside of the post-perovskite stability field. Therefore, the particle path lengths and strain rates sampled are affected by the Clapeyron slope and pressure intercept we chose. We used a Clapeyron slope which is within the range of estimates from experiments and calculations (Hirose et al., 2015; Kuwayama et al., 2022). By assuming pure post-perovskite, we do not account for any additional phases such as ferropericlase or bridgmanite which may strengthen or weaken the anisotropy depending on if and how texture may develop. Furthermore, effects such as those from strain localisation are not accounted for.

5. Conclusion

We tested the sensitivity of present-day lowermost mantle anisotropy to past mantle flow by comparing the anisotropy predicted from two mantle flow field models: one where the flow field varies with time and another where the flow is constant. As texture and anisotropy are controlled by both the flow field and slip system activities we create three test cases where we vary the ease-of-texturing to test for its impact. We find, in all ease-of-texturing cases, low-resolution observations such as 1-D radial anisotropy observations and seismic tomography are likely sensitive to present-day flow only. High-resolution regional observations, such as those from shear-wave splitting, may hold some information about past mantle flow. If the resolution of seismic tomography improves, it may also have some sensitivity to past flow. Varying the ease-of-texturing of the crystal aggregate leads to a similar spatial distribution but the easier-to-texture material leads to greater differences in the anisotropy between the flow field cases at some locations. We investigate what could contribute to the impact of past flow on present-day

anisotropy. We find path properties such as differences in path length and tortuosity between the flow fields show the strongest correlation with anisotropy difference. We also find the temperature at the endpoint may also have an effect with hotter temperatures leading to larger differences between the predicted anisotropy from a time-varying and constant flow field. From this, we conclude there is no one dominant predictor of sensitivity to past flow. Ultimately, we show that low-resolution observations of lower mantle anisotropy such as those from current seismic tomography or 1D radial anisotropy estimates are sensitive to present-day flow alone. This implies that inversions of flow from such observations may give promising estimates of present-day convection patterns. Regional, high-resolution observations such as those from shear-wave splitting may provide some sensitivity to historic flow. As constraints on mineral physics and deformation mechanisms in D′′ are tightened in the future, our work gives us confidence that inversions for recent mantle flow from seismic anisotropy observations may become possible in time.

Acknowledgements

All authors are supported by NERC large grant 'Mantle Circulation Constrained' (JW, AW and AN: NE/T012684/1; JP and JHD: NE/T012633/1). AN is partly funded by NERC standard grant 'REMIS: Reliable Earthquake Magnitudes for Induced Seismicity' (NE/R001154/1). Figures were made using Matplotlib (Hunter, 2007) and cartopy (Met Office, 2010 - 2015). Code to perform the seismic anisotropy calculation from flow is available upon request.

References

Ammann, M., Brodholt, J., Wookey, J., Dobson, D., 2010. First-principles constraints on diffusion in lower-mantle minerals and a weak D′′ layer. Nature 465, 462–465.

Asplet, J., Wookey, J., Kendall, M., 2020. A potential post-perovskite province in D′′ beneath the Eastern Pacific: evidence from new analysis of discrepant SKS–SKKS shear wave splitting. Geophysical Journal International 221, 2075–2090.

Auer, L., Boschi, L., Becker, T., Nissen-Meyer, T., Giardini, D., 2014. Savani: A variable resolution whole-mantle model of anisotropic shear velocity variations based on multiple data sets. Journal of Geophysical Research: Solid Earth 119, 3006–3034.

Baumgardner, J.R., 1985. Three-dimensional treatment of convective flow in the earth's mantle. Journal of Statistical Physics 39, 501–511. doi:10.1007/BF01008348.

Boioli, F., Carrez, P., Cordier, P., Devincre, B., Gouriet, K., Hirel, P., Kraych, A., Ritterbex, S., 2017. Pure climb creep mechanism drives flow in Earth's lower mantle. Science Advances 3, e1601958.

Browaeys, J.T., Chevrot, S., 2004. Decomposition of the elastic tensor and geophysical applications. Geophysical Journal International 159, 667–678.

Bunge, H.P., Richards, M.A., Baumgardner, J.R., 1997. A sensitivity study of three-dimensional spherical mantle convection at 10 8 Rayleigh number: Effects of depth-dependent viscosity, heating mode, and an endothermic phase change. Journal of Geophysical Research: Solid Earth 102, 11991–12007. doi:10.1029/96JB03806. iSBN: 0148-0227.

Chandler, B.C., Chen, L.W., Li, M., Romanowicz, B., Wenk, H.R., 2021. Seismic anisotropy, dominant slip systems and phase transitions in the lowermost mantle. Geophysical Journal International 227, 1665–1681.

Chang, S.J., Ferreira, A.M., Ritsema, J., van Heijst, H.J., Woodhouse, J.H., 2014. Global radially anisotropic mantle structure from multiple datasets: a review, current challenges, and outlook. Tectonophysics 617, 1–19.

Cottaar, S., Li, M., McNamara, A.K., Romanowicz, B., Wenk, H.R., 2014. Synthetic seismic anisotropy models within a slab impinging on the core–mantle boundary. Geophysical Journal International 199, 164–177.

Cottaar, S., Romanowicz, B., 2013. Observations of changing anisotropy across the southern margin of the African LLSVP. Geophysical Journal International 195, 1184–1195.

Davies, D.R., Goes, S., Davies, J.H., Schuberth, B., Bunge, H.P., Ritsema, J., 2012a. Reconciling dynamic and seismic models of Earth's lower mantle: The dominant role of thermal heterogeneity. Earth and Planetary Science Letters 353, 253–269.

Davies, D.R., Goes, S., Davies, J.H., Schuberth, B.S.A., Bunge, H.P., Ritsema, J., 2012b. Reconciling dynamic and seismic models of Earth's lower mantle: The dominant role of thermal heterogeneity. Earth and Planetary Science Letters 353-354, 253–269. doi:10.1016/j.epsl.2012.08.016. publisher: Elsevier ISBN: 0012-821X.

Davies, J.H., Davies, D.R., 2010. Earth's surface heat flux. Solid Earth 1, 5–24.

De Wit, R., Trampert, J., 2015. Robust constraints on average radial lower mantle anisotropy and consequences for composition and texture. Earth and Planetary Science Letters 429, 101–109.

Deschamps, F., Cobden, L., 2022. Estimating core-mantle boundary temperature from seismic shear velocity and attenuation. Frontiers in Earth Science 10, 1031507.

Dobson, D.P., Lindsay-Scott, A., Hunt, S.A., Bailey, E., Wood, I.G., Brodholt, J.P., Vocadlo, L., Wheeler, J., 2019. Anisotropic diffusion creep in postperovskite provides a new model for deformation at the core- mantle boundary. Proceedings of the National Academy of Sciences 116, 26389–26393.

Gorski, K.M., Hivon, E., Banday, A.J., Wandelt, B.D., Hansen, F.K., Reinecke, M., Bartelmann, M., 2005. HEALPix: A framework for high-resolution discretization and fast analysis of data distributed on the sphere. The Astrophysical Journal 622, 759.

Hansen, L., Zimmerman, M., Kohlstedt, D., 2012. Laboratory measurements of the viscous anisotropy of olivine aggregates. Nature 492, 415–418.

van Heck, H.J., Davies, J.H., Elliott, T., Porcelli, D., 2016. Global-scale modelling of melting and isotopic evolution of Earth's mantle: Melting modules for TERRA. Geoscientific Model Development 9, 1399–1411. doi:10.5194/gmd-9-1399-2016.

Hirose, K., Wentzcovitch, R., Yuen, D., Lay, T., 2015. Mineralogy of the deep mantle—The post-perovskite phase and its geophysical significance. Treatise on Geophysics , 85–115.

Hunter, J.D., 2007. Matplotlib: A 2D graphics environment. Computing in Science & Engineering 9, 90–95. doi:10.1109/MCSE.2007.55.

van Keken, P.E., Ballentine, C.J., 1998. Whole-mantle versus layered mantle convection and the role of a high-viscosity lower mantle in terrestrial volatile evolution. Earth and Planetary Science Letters 156, 19–32. doi:10.1016/s0012-821x(98)00023-5.

Kennett, B.L., Engdahl, E., Buland, R., 1995. Constraints on seismic velocities in the Earth from traveltimes. Geophysical Journal International 122, 108–124.

Kim, T., Ko, B., Greenberg, E., Prakapenka, V., Shim, S.H., Lee, Y., 2020. Low melting temperature of anhydrous mantle materials at the core-mantle boundary. Geophysical Research Letters 47, e2020GL089345.

Kuwayama, Y., Hirose, K., Cobden, L., Kusakabe, M., Tateno, S., Ohishi, Y., 2022. Post-perovskite phase transition in the pyrolitic lowermost mantle: Implications for ubiquitous occurrence of post-perovskite above CMB. Geophysical Research Letters 49, e2021GL096219.

Labrosse, S., Jaupart, C., 2007. Thermal evolution of the Earth : Secular changes and fluctuations of plate characteristics. Earth and Planetary Science Letters 260, 465–481. doi:10.1016/j.epsl.2007.05.046.

Lebensohn, R.A., Tomé, C., 1993. A self-consistent anisotropic approach for the simulation of plastic deformation and texture development of polycrystals: application to zirconium alloys. Acta metallurgica et materialia 41, 2611–2624.

Li, Y., Deschamps, F., Tackley, P.J., 2014. Effects of low-viscosity post-perovskite on the stability and structure of primordial reservoirs in the lower mantle. Geophysical Research Letters 41, 7089–7097.

Lobanov, S.S., Speziale, S., Brune, S., 2021. Modelling Mie scattering in pyrolite in the laser-heated diamond anvil cell: Implications for the core-mantle boundary temperature determination. Physics of the Earth and Planetary Interiors 318, 106773.

Magali, J.K., Bodin, T., Hedjazian, N., Samuel, H., Atkins, S., 2021. Geodynamic tomography: Constraining upper-mantle deformation patterns from

Bayesian inversion of surface waves. Geophysical Journal International 224, 2077–2099. doi:10.1093/gji/ggaa577.

Mameri, L., Tommasi, A., Signorelli, J., Hansen, L.N., 2019. Predicting viscoplastic anisotropy in the upper mantle: a comparison between experiments and polycrystal plasticity models. Physics of the Earth and Planetary Interiors 286, 69–80.

McKenzie, D.P., Roberts, J.M., Weiss, N.O., 1974. Convection in the earth's mantle: Towards a numerical simulation. Journal of Fluid Mechanics 62, 465–538. doi:10.1017/S0022112074000784. iSBN: 0022-1120.

McNamara, A.K., Karato, S.I., Van Keken, P.E., 2001. Localization of dislocation creep in the lower mantle: implications for the origin of seismic anisotropy. Earth and Planetary Science Letters 191, 85–99.

McNamara, A.K., van Keken, P.E., Karato, S.I., 2003. Development of finite strain in the convecting lower mantle and its implications for seismic anisotropy. Journal of Geophysical Research: Solid Earth 108.

McNamara, A.K., Van Keken, P.E., Karato, S.I., 2002. Development of anisotropic structure in the Earth's lower mantle by solid-state convection. Nature 416, 310–314.

Merdith, A.S., Williams, S.E., Collins, A.S., Tetley, M.G., Mulder, J.A., Blades, M.L., Young, A., Armistead, S.E., Cannon, J., Zahirovic, S., Müller, R.D., 2020. Extending full-plate tectonic models into deep time: Linking the neoproterozoic and the phanerozoic. Earth-Science Reviews 214, 103477. doi:10.1016/j.earscirev.2020.103477. publisher: Elsevier BV.

Merkel, S., McNamara, A.K., Kubo, A., Speziale, S., Miyagi, L., Meng, Y., Duffy, T.S., Wenk, H.R., 2007. Deformation of (Mg,Fe)SiO_3 post-perovskite and D″ anisotropy. Science 316, 1729–1732.

Met Office, 2010 - 2015. Cartopy: a cartographic python library with a Matplotlib interface. Exeter, Devon. URL: `https://scitools.org.uk/cartopy`.

Miyagi, L., Kanitpanyacharoen, W., Kaercher, P., Lee, K.K., Wenk, H.R., 2010. Slip systems in $MgSiO_3$ post-perovskite: Implications for D″ anisotropy. Science 329, 1639–1641.

Nowacki, A., Cottaar, S., 2021. Toward imaging flow at the base of the mantle with seismic, mineral physics, and geodynamic constraints. Mantle Convection and Surface Expressions , 329–352.

Nowacki, A., Walker, A.M., Wookey, J., Kendall, J.M., 2013. Evaluating post-perovskite as a cause of D″ anisotropy in regions of palaeosubduction. Geophysical Journal International 192, 1085–1090.

Nowacki, A., Wookey, J., 2016. The limits of ray theory when measuring shear wave splitting in the lowermost mantle with ScS waves. Geophysical Journal International 207, 1573–1583.

Nowacki, A., Wookey, J., J-Michael, K., 2010. Deformation of the lowermost mantle from seismic anisotropy. Nature , 1091–1094.

Nowacki, A., Wookey, J., Kendall, J.M., 2011. New advances in using seismic anisotropy, mineral physics and geodynamics to understand deformation in the lowermost mantle. Journal of Geodynamics 52, 205–228. doi:10.1016/j.jog.2011.04.003.

Panton, J., Davies, J.H., Myhill, R., 2023. The Stability of Dense Oceanic Crust Near the Core-Mantle Boundary. Journal of Geophysical Research: Solid Earth 128, e2022JB025610. doi:10.1029/2022JB025610.

Park, Y., Azuma, S., Okazaki, K., Uesugi, K., Yasutake, M., Nishihara, Y., Nomura, R., 2022. Development of Lattice-Preferred Orientations of MgO Periclase From Strain Rate Controlled Shear Deformation Experiments Under Pressure up to 120 GPa. Geophysical Research Letters 49, e2022GL100178.

Reali, R., Van Orman, J.A., Pigott, J.S., Jackson, J.M., Boioli, F., Carrez, P., Cordier, P., 2019. The role of diffusion-driven pure climb creep on the rheology of bridgmanite under lower mantle conditions. Scientific Reports 9, 2053.

Restelli, F., Koelemeijer, P., Ferreira, A., 2023. Normal mode observability of radial anisotropy in the Earth's mantle. Geophysical Journal International 233, 663–679.

Silver, P.G., Chan, W.W., 1991. Shear wave splitting and subcontinental mantle deformation. Journal of Geophysical Research: Solid Earth 96, 16429–16454.

Simmons, N., Myers, S., Morency, C., Chiang, A., Knapp, D., 2021. SPiRaL: a multiresolution global tomography model of seismic wave speeds and radial anisotropy variations in the crust and mantle. Geophysical Journal International 227, 1366–1391.

Stackhouse, S., Brodholt, J.P., 2007. The high-temperature elasticity of MgSiO 3 post-perovskite. Washington DC American Geophysical Union Geophysical Monograph Series 174, 99–113.

Stackhouse, S., Brodholt, J.P., Wookey, J., Kendall, J.M., Price, G.D., 2005. The effect of temperature on the seismic anisotropy of the perovskite and post-perovskite polymorphs of $MgSiO_3$. Earth and Planetary Science Letters 230, 1–10.

Walker, A., Forte, A., Wookey, J., Nowacki, A., Kendall, J.M., 2011. Elastic anisotropy of D″ predicted from global models of mantle flow. Geochemistry, Geophysics, Geosystems 12.

Walker, A.M., Dobson, D.P., Wookey, J., Nowacki, A., Forte, A.M., 2018. The anisotropic signal of topotaxy during phase transitions in D″. Physics of the Earth and Planetary Interiors 276, 159–171.

Wenk, H.R., Cottaar, S., Tomé, C.N., McNamara, A., Romanowicz, B., 2011. Deformation in the lowermost mantle: From polycrystal plasticity to seismic anisotropy. Earth and Planetary Science Letters 306, 33–45.

Wenk, H.R., Speziale, S., McNamara, A., Garnero, E., 2006. Modeling lower mantle anisotropy development in a subducting slab. Earth and Planetary Science Letters 245, 302–314.

Wentzcovitch, R.M., Tsuchiya, T., Tsuchiya, J., 2006. MgSiO3 postperovskite at D″ conditions. Proceedings of the National Academy of Sciences 103, 543–546.

Wheeler, J., 2009. The preservation of seismic anisotropy in the Earth's mantle during diffusion creep. Geophysical Journal International 178, 1723–1732.

Wolf, J., Frost, D.A., Long, M.D., Garnero, E., Aderoju, A.O., Creasy, N., Bozdağ, E., 2023a. Observations of mantle seismic anisotropy using array techniques: Shear-wave splitting of beamformed SmKS phases. Journal of Geophysical Research: Solid Earth 128, e2022JB025556.

Wolf, J., Long, M.D., Li, M., Garnero, E., 2023b. Global compilation of deep mantle anisotropy observations and possible correlation with low velocity provinces. Geochemistry, Geophysics, Geosystems 24, e2023GC011070.

Wookey, J., Kendall, J.M., Rümpker, G., 2005. Lowermost mantle anisotropy beneath the north Pacific from differential S—ScS splitting. Geophysical Journal International 161, 829–838.

Supplementary material for "The sensitivity of lowermost mantle anisotropy to past mantle convection"

James Ward[a,1], Andrew M. Walker[b], Andy Nowacki[a,*], James Panton[c], J. Huw Davies[c]

[a]*School of Earth and Environment, University of Leeds, Leeds, LS2 9JT, West Yorkshire, United Kingdom*
[b]*Department of Earth Sciences, University of Oxford, Oxford, OX1 3AN, Oxfordshire, United Kingdom*
[c]*School of Earth and Environmental Sciences, Cardiff University, Cardiff, CF10 3AT, Cardiff, United Kingdom*

1. Supplementary figures

In this supplementary material we include additional figures showing radial P-wave anisotropy for all ease-of-texture cases (Figure S1), comparisons between radial anisotropy for the two flow models (Figs. S2–S7) and cumulative histograms of radial anisotropy values (Figs. S8 and S9).

*Corresponding author: a.nowacki@leeds.ac.uk
[1]Now at HM Government Statistical Service

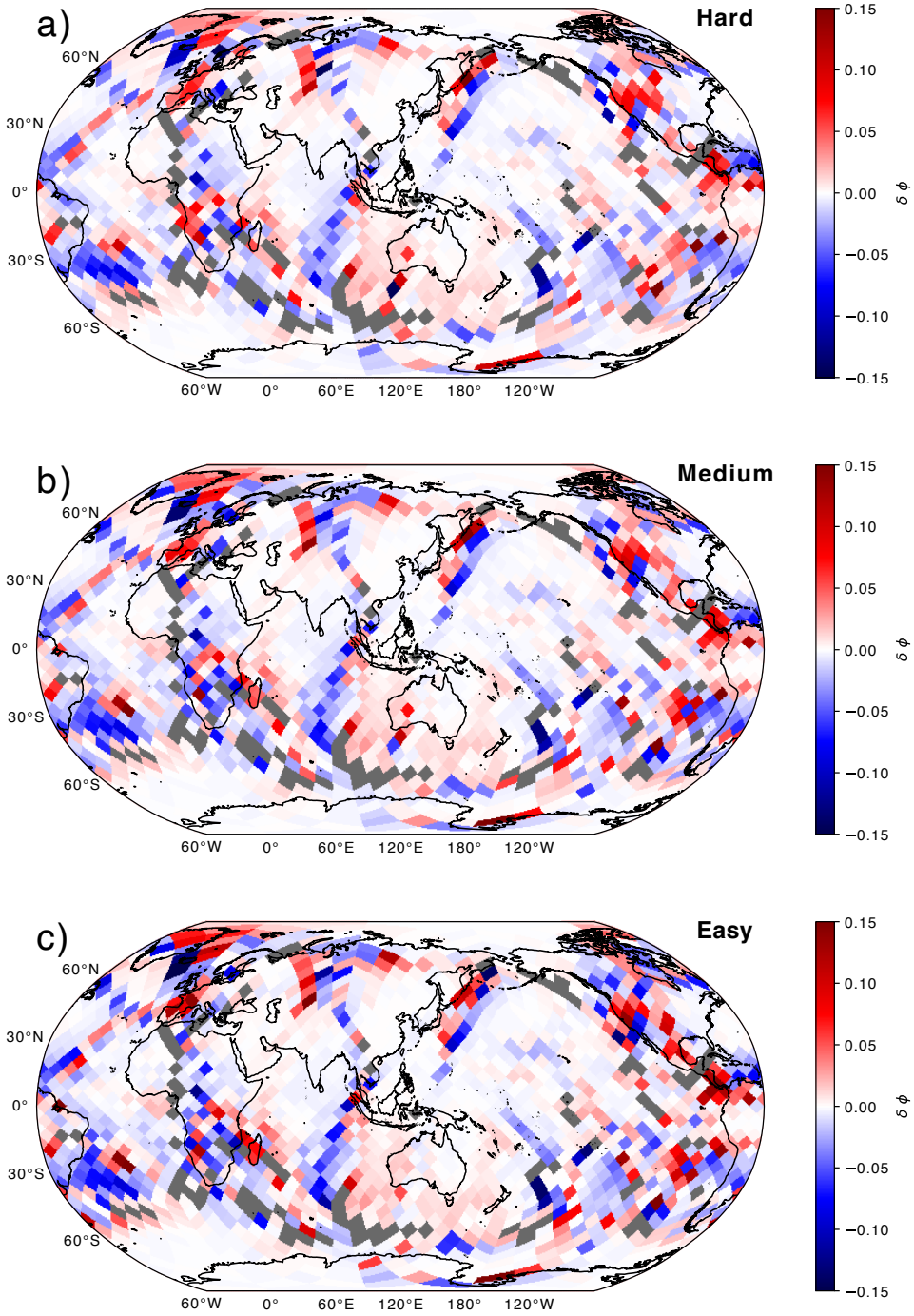

Figure S1: Maps showing the difference between P-wave radial anisotropy (ϕ) at 3530 km radius (50 km above the core–mantle boundary) for the different flow fields with the different ease-of-texturing cases. The regions in grey show where post-perovskite is not predicted to be stable at this depth.

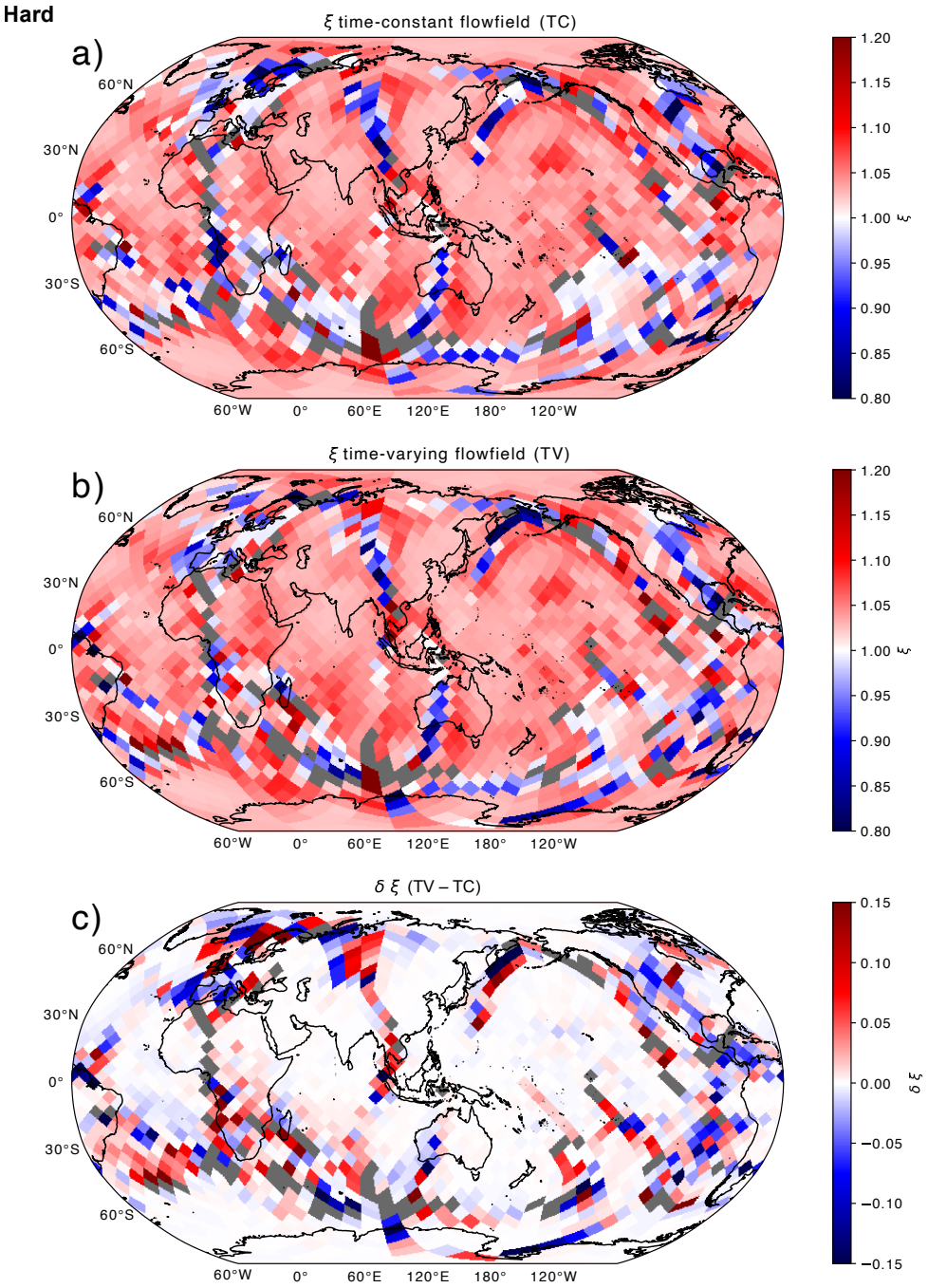

Figure S2: Maps of S-wave radial anisotropy (ξ) at 3530 km radius (50 km above the core–mantle boundary) for the *hard-to-texture case*. We show ξ calculated with the time-constant (TC) flowfield (a), the time-varying (TV) flowfield (b) and the difference between the two (c).

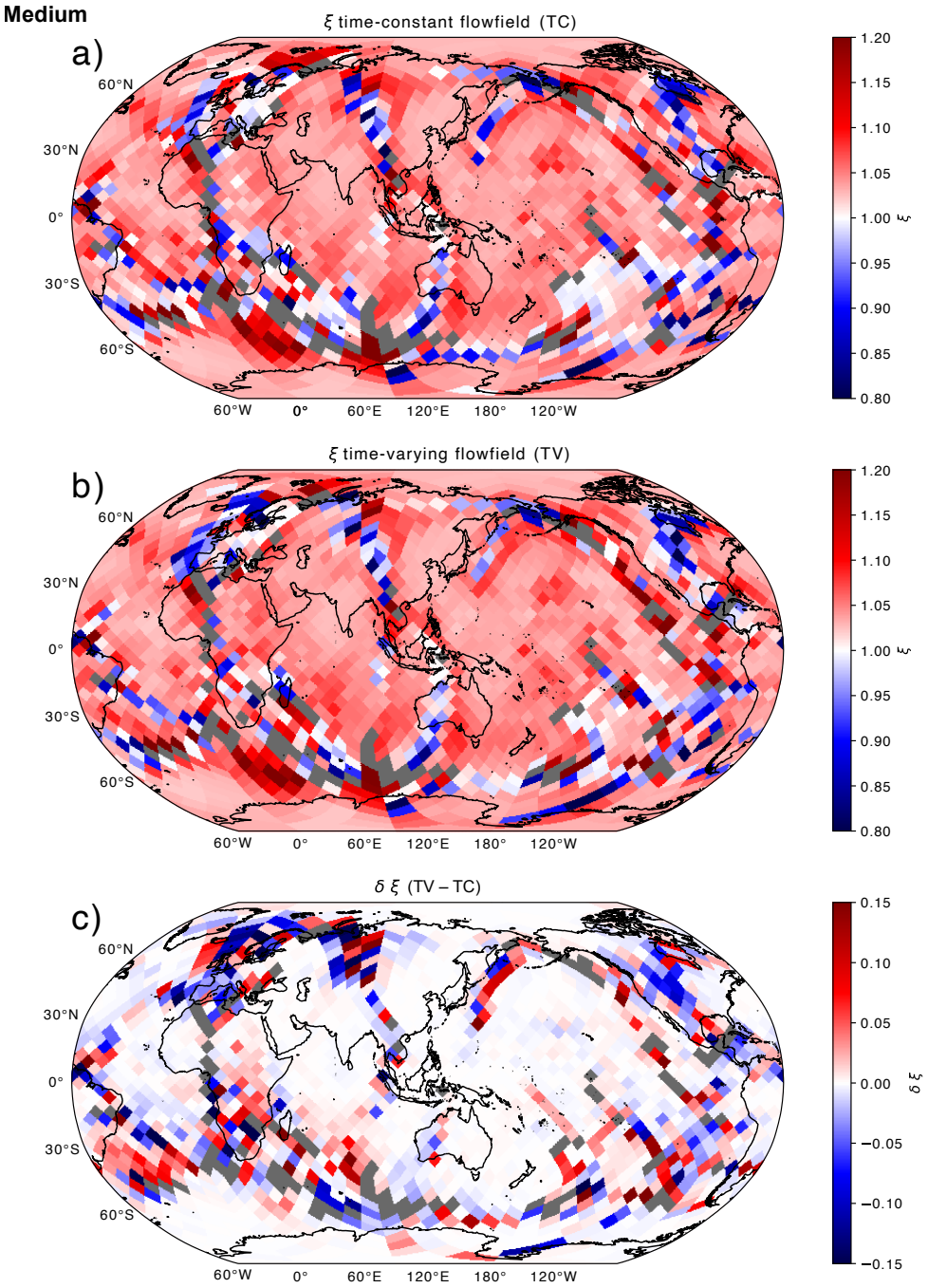

Figure S3: Maps of S-wave radial anisotropy (ξ) at 3530 km radius (50 km above the core–mantle boundary) for the *medium texture case*. We show ξ calculated with the time-constant (TC) flowfield (a), the time-varying (TV) flowfield (b) and the difference between the two (c).

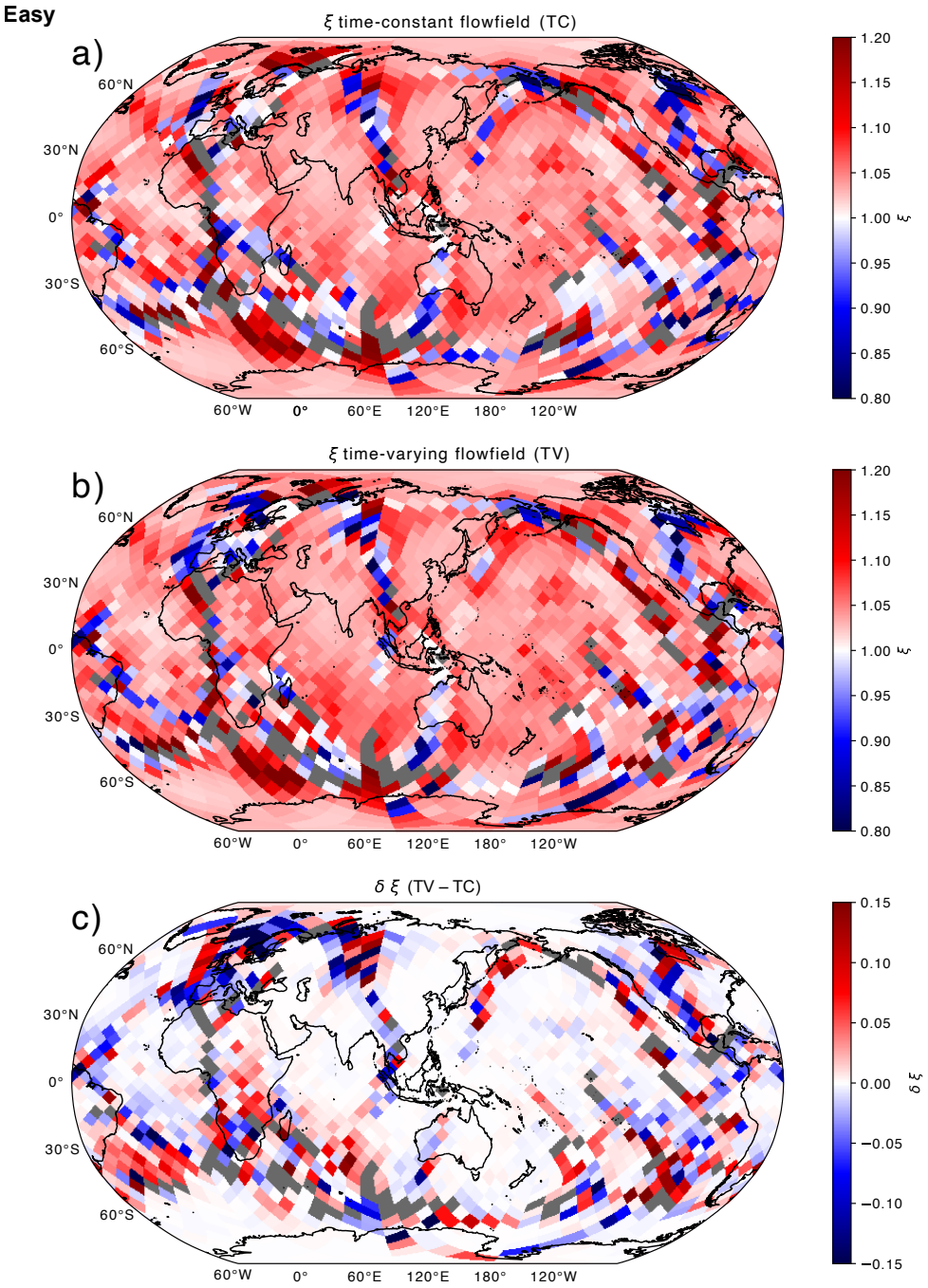

Figure S4: Maps of S-wave radial anisotropy (ξ) at 3530 km radius (50 km above the core–mantle boundary) for the *easy-to-texture case*. We show ξ calculated with the time-constant (TC) flowfield (a), the time-varying (TV) flowfield (b) and the difference between the two (c).

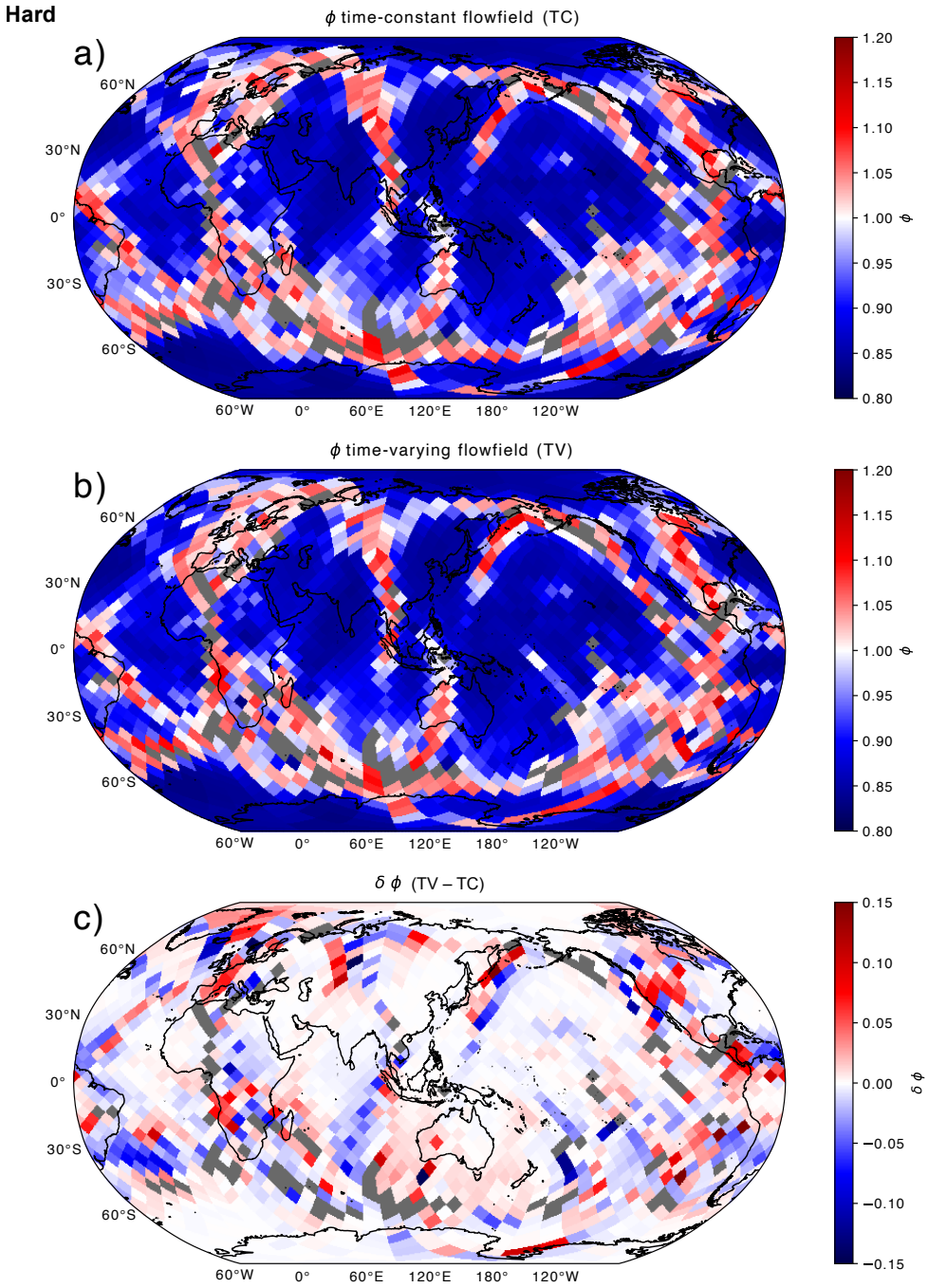

Figure S5: Maps of P-wave radial anisotropy (ϕ) at 3530 km radius (50 km above the core–mantle boundary) for the *hard-to-texture case*. We show ϕ calculated with the time-constant (TC) flowfield (a), the time-varying (TV) flowfield (b) and the difference between the two (c).

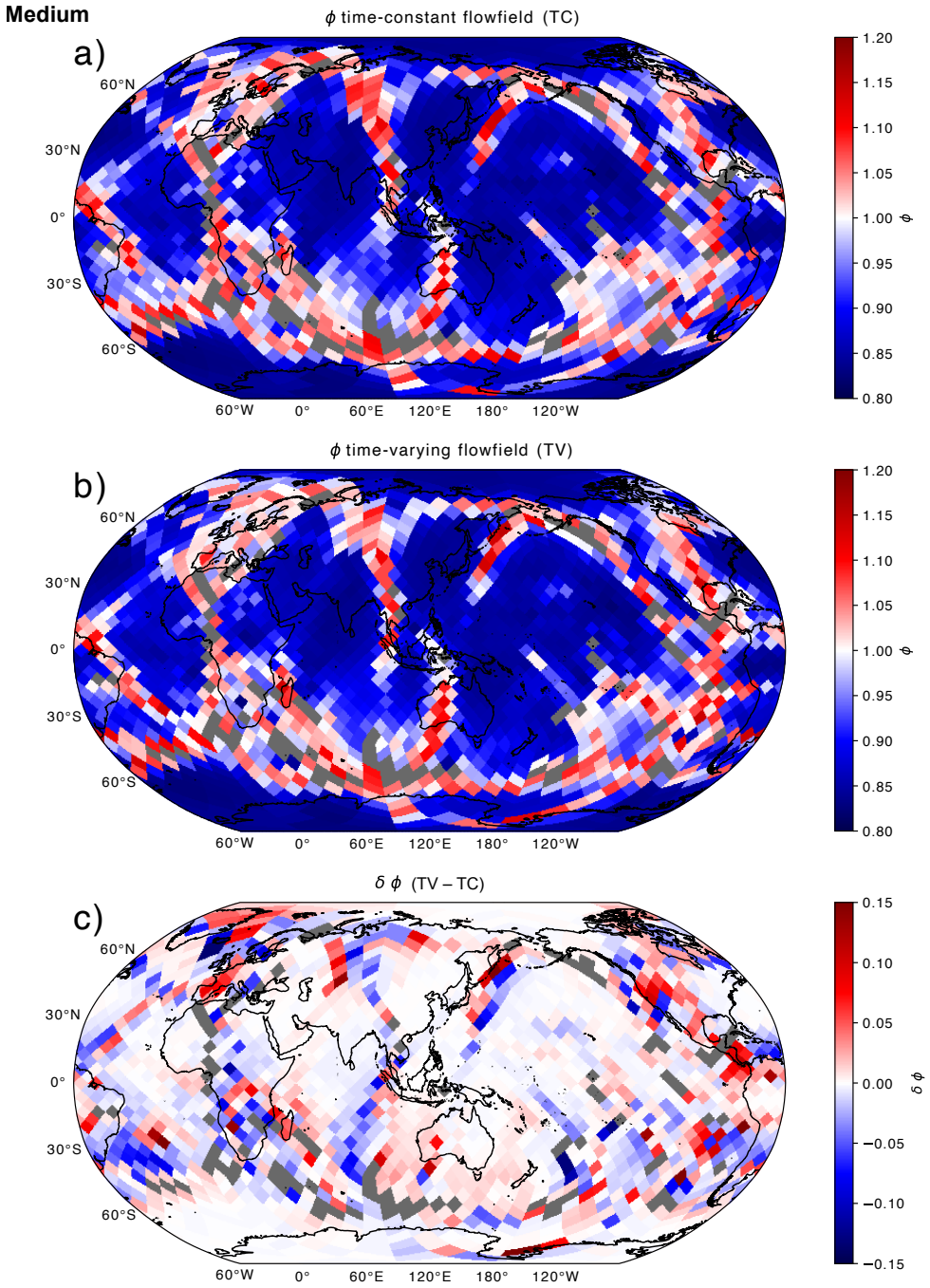

Figure S6: Maps of P-wave radial anisotropy (ϕ) at 3530 km radius (50 km above the core–mantle boundary) for the *medium texture case*. We show ϕ calculated with the time-constant (TC) flowfield (a), the time-varying (TV) flowfield (b) and the difference between the two (c).

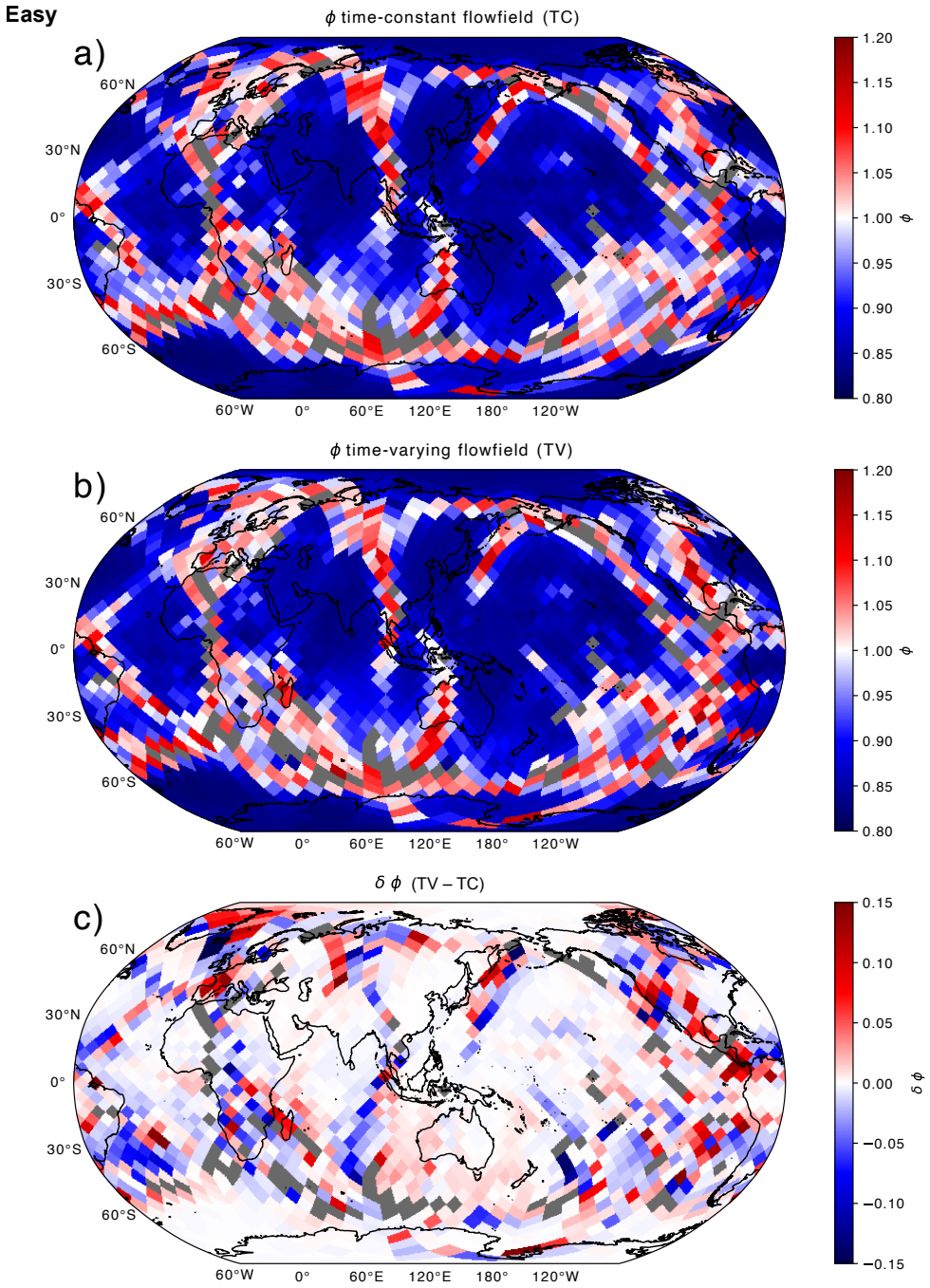

Figure S7: Maps of P-wave radial anisotropy (ϕ) at 3530 km radius (50 km above the core–mantle boundary) for the *easy-to-texture case*. We show ϕ calculated with the time-constant (TC) flowfield (a), the time-varying (TV) flowfield (b) and the difference between the two (c).

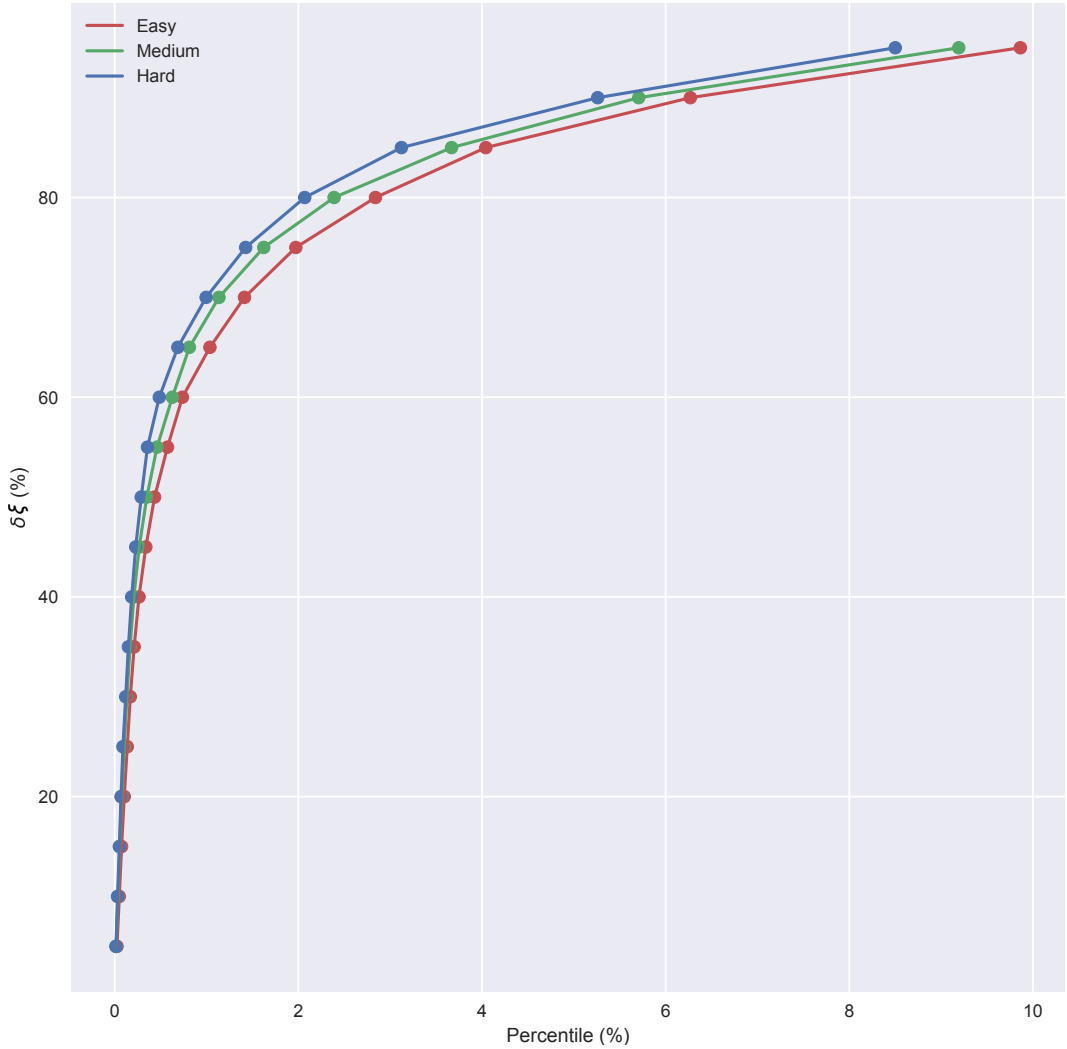

Figure S8: Cumulative histograms showing the effect of slip system activities on the sensitivity of ξ observations to past flow in the lower mantle. This figure shows the different percentile ξ values coloured by the slip system label from Table 2 (main text). Notice at the larger percentiles the easy-to-texture case always has larger differences in ξ between the flow fields.

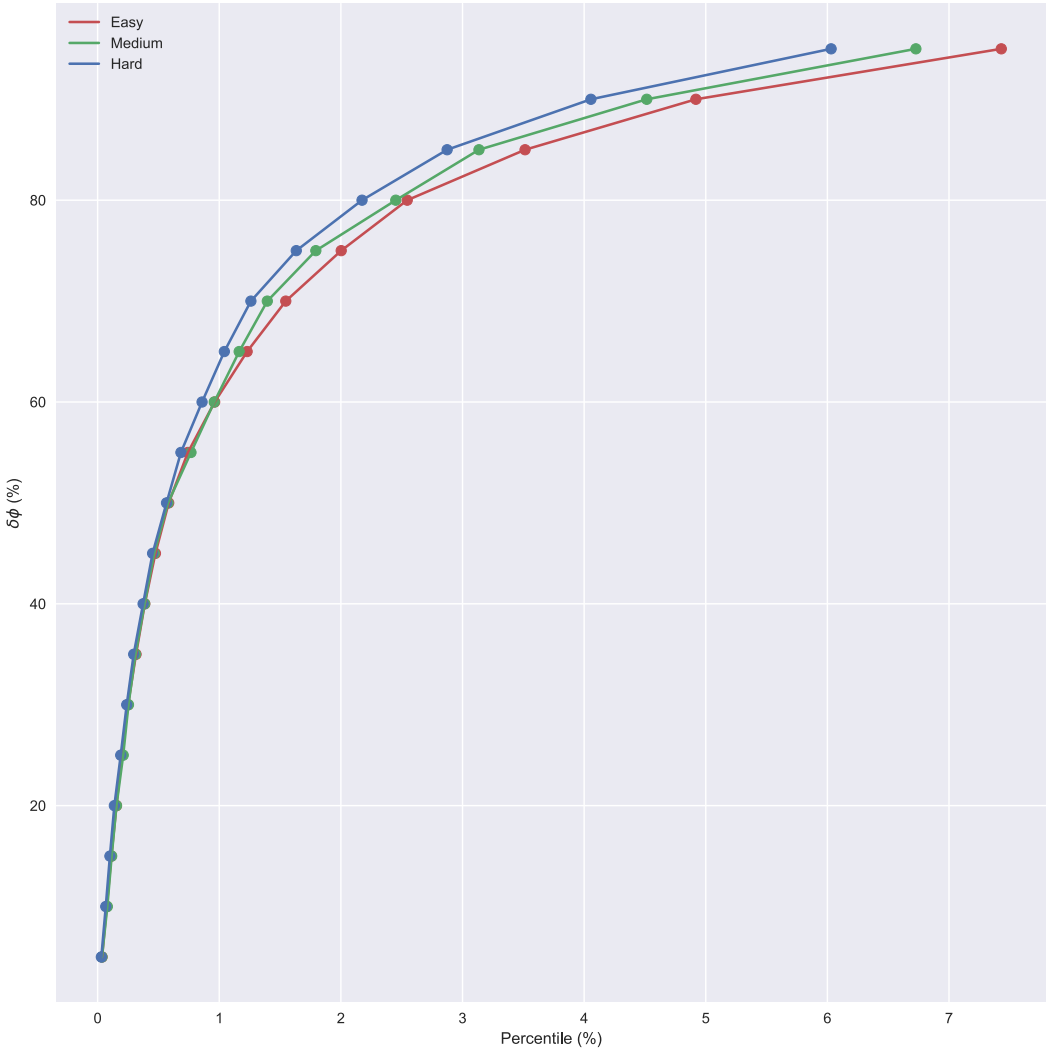

Figure S9: Cumulative histograms showing the effect of slip system activities on the sensitivity of ϕ observations to past flow in the lower mantle. This figure shows the different percentile ϕ values coloured by the slip system label from Table 2 (main text). Notice at the larger percentiles the easy-to-texture case always has larger differences in ϕ between the flow fields.